



## RESEARCH ARTICLE

10.1029/2023JD038956

# Analysis of Trapped Small-Scale Internal Gravity Waves Automatically Detected in Satellite Imagery

R. Vicari<sup>1,2</sup> , C. C. Stephan<sup>3</sup> , T. P. Lane<sup>1</sup> , and Y. Huang<sup>1</sup> 

<sup>1</sup>School of Geography, Earth and Atmospheric Sciences, and ARC Centre of Excellence for Climate Extremes, The University of Melbourne, Melbourne, Victoria, Australia, <sup>2</sup>International Max Planck Research School on Earth System Modelling, Hamburg, Germany, <sup>3</sup>Max Planck Institute for Meteorology, Hamburg, Germany

### Key Points:

- Water vapor-sensitive satellite imagery contains signatures of trapped internal waves that can be automatically detected
- Over the eastern tropical Pacific, trapped internal waves in the upper troposphere are more likely during December, January, and February
- The increased likelihood is due to sub-seasonal intermittent absolute wind shear in combination with a more steady small buoyancy frequency

### Correspondence to:

R. Vicari,  
rvicari@student.unimelb.edu.au

### Citation:

Vicari, R., Stephan, C. C., Lane, T. P., & Huang, Y. (2024). Analysis of trapped small-scale internal gravity waves automatically detected in satellite imagery. *Journal of Geophysical Research: Atmospheres*, 129, e2023JD038956. <https://doi.org/10.1029/2023JD038956>

Received 11 APR 2023  
Accepted 11 DEC 2023

**Abstract** In water vapor-sensitive satellite imagery, small-scale wave-like perturbations of brightness temperature can be attributed to the presence of trapped internal waves in the troposphere. We present a method for detecting these local perturbations with wavelengths of about 10 km and apply it to imagery from the Advanced Baseline Imager on board the geostationary satellite GOES-16. The algorithm allows us to analyze 4 years of sub-hourly data in the southern part of the tropical eastern Pacific, where only a relatively low amount of medium and high clouds obscures the scene. By combining a measure of wave activity/trapping with ERA5 reanalysis data, we connect the occurrence of trapping with the presence of an increased upper-tropospheric wind shear. This connection is more evident during December, January and February, when upper-tropospheric jets are more likely. Our work supports existing case and model studies and is a step forward in the statistical and automated analysis of trapped small-scale internal waves in the atmosphere.

**Plain Language Summary** Remote sensing instruments on satellites are able to measure the electromagnetic energy emitted by the Earth and the atmosphere. Certain wavelength ranges of the electromagnetic energy, called channels or bands of the respective instrument, can be related to relative humidity. Depending on the channel, these layers cover primarily the middle or the upper troposphere. Since atmospheric small-scale waves influence the vertical structure of relative humidity, we analyze the resulting local horizontal variability in the satellite observations. We automatically detect these patterns over the eastern Pacific and explain why and when they occur during the season. Our work contributes to the identification of processes in the troposphere that can lead to hazardous weather.

## 1. Introduction

Tropospheric small-scale internal waves (TSIW), that is, internal (buoyancy/gravity) waves in the troposphere with horizontal wavelengths of the order of 10 km, can be vertically reflected and constructively interfere under certain background conditions. These conditions include vertical changes in stability, shear and wind curvature, all of which can affect the ability of waves to propagate vertically. Such changes in the background state can lead to dissipation of waves, for example, wave breaking, wave reflection potentially leading to “trapping”, and other filtering mechanisms, for example, evanescence or exponential decay. Full descriptions of these mechanisms can be found in Nappo (2012). The trapping mechanism can affect tropospheric phenomena related to vertical velocity, such as (a) boundary layer thermals, (b) cirrus cloud formation, (c) vertical mixing, and (d) turbulence, as follows:

- In idealized high-resolution simulations (Balaji & Clark, 1988; Balaji et al., 1993; Clark et al., 1986; Lane & Clark, 2002), it has been noted that trapped TSIW can modulate the horizontal spacing of the boundary layer thermals to match their dominant horizontal wavelengths. This is particularly important because boundary layer thermals generate TSIW by penetrating into the stable troposphere aloft (Böhme et al., 2004, 2007; Gibert et al., 2011; Hauf, 1993; Kuettner et al., 1987), creating a potential feedback on themselves as seen in the simulations mentioned. In two of the simulations (Balaji & Clark, 1988; Balaji et al., 1993), it has further been found that the increased spacing of the thermals even allowed the development of deeper convective cells. In a coarser (~2.4 km) but more realistic simulation (Stephan, 2020), a coupling between trapped TSIW and the cloud field has been seen.
- It is known that TSIW can influence the formation and evolution of cirrus clouds by increasing cooling rates and thus ice concentrations (Dinh et al., 2016; Jensen et al., 2016; Schoeberl et al., 2015; Spichtinger

© 2024 The Authors.

This is an open access article under the terms of the [Creative Commons Attribution-NonCommercial License](https://creativecommons.org/licenses/by-nc/4.0/), which permits use, distribution and reproduction in any medium, provided the original work is properly cited and is not used for commercial purposes.

- & Krämer, 2013). In addition to the effect of temperature variability, the spatial confinement of ice crystals caused by TSIW motion has been investigated in Podglajen et al. (2018).
- (c) For example, the studies of Moustouli et al. (2010) and Heller et al. (2017) suggest that TSIW generated by mountains can contribute to a nonzero vertical net flux of trace gases, including moisture, and irreversible mixing in the upper troposphere-lower stratosphere.
  - (d) Uhlenbrock et al. (2007) have been able to link severe turbulence reported by pilots to the presence of horizontally trapped TSIW generated by mountains. These results have been extended in Wimmers et al. (2018) by further observational cases. It is known that trapped internal waves can further amplify a turbulent environment (Lane et al., 2012; Trier & Sharman, 2018).

With respect to the above phenomena (a)–(d), the aim of the present work is to identify the primary physical cause of TSIW trapping in the real atmosphere. Since inference of local causality is inconclusive or even impossible with current observations, we limit ourselves to the question of which tropospheric background state increases the likelihood of TSIW trapping. The main advance of the present work is the combined large-scale analysis of satellite observations and reanalysis data, which overcomes case-by-case studies (e.g., Feltz et al., 2009; Uhlenbrock et al., 2007; Wimmers et al., 2018), and thus provides a test of results obtained by existing observational and model studies. We algorithmically link TSIW trapping signatures in water vapor-sensitive satellite imagery with reanalysis data over 4 consecutive years within a domain size of about  $10^7 \text{ km}^2$  over the eastern tropical Pacific. This allows us, based on existing theory, to attribute the increased occurrence of signatures to an increase in absolute horizontal wind shear  $|(\partial_z u, \partial_z v)|$  around a pressure level of 325 hPa, an altitude of about 9 km. The increase in absolute horizontal wind shear is due to jets aloft, inducing a reflection layer that is vertically bounded by the relatively more invariant but vertically decreasing buoyancy frequency. Since upper-tropospheric jets over the eastern tropical Pacific are more common during the boreal winter in December, January and February (DJF), there is also a season of increased TSIW trapping.

A well-established condition for vertical trapping of internal waves in the framework of linear theory is  $l^2 < k^2$  (Nappo, 2012), where  $k$  is the horizontal wavenumber of an internal wave and  $l$  is the Scorer parameter. The Scorer parameter  $l$ , derived from the Taylor-Goldstein equation describing linear wave motion, is defined by

$$l^2 = (u - c)^{-2} \cdot \left( N^2 - (u - c) \cdot (\partial_z^2 u - H_s^{-1} \partial_z u) \right) - (2 H_s)^{-2} \quad (1)$$

where  $u$  is the horizontal wind in the direction of the internal wave propagation,  $c$  the ground-based phase velocity of the internal wave and  $H_s$  the density scale height. Using the notation in Stephan (2020, Section 3a), this condition can be equivalently expressed through the “critical wavelength”  $\lambda_* = 2\pi \cdot l^{-1}$ , which indicates the reflection of internal waves when  $\lambda < \lambda_*$ , where  $\lambda$  is the horizontal wavelength of the internal wave. The singularity of  $l^2$ , namely  $u = c$ , is called a critical level. In linear theory, internal waves dissipate when they reach a critical level.

While linear theory predicts wave energy absorption at critical levels, it is known that for a small Richardson number  $\text{Ri} := N^2 \cdot |(\partial_z u, \partial_z v)|^{-2}$ , waves are also reflected in the vicinity of critical levels (Teixeira, 2014). The Richardson number  $\text{Ri}$  quantifies the stability of the flow affected by the stratification, that is, the buoyancy frequency  $N$ , and the wind shear  $|(\partial_z u, \partial_z v)|$ . While for  $\text{Ri} \gg 1$  the processes are in line with linear theory, this changes if  $\text{Ri} < 1$  resulting in substantial wave reflection (Teixeira, 2014). Especially abruptly changing horizontal wind resulting in a sudden decrease of  $\text{Ri}$  is known to induce reflection layers (Teixeira & Argañ, 2020; Teixeira et al., 2005). However,  $\text{Ri}$  is in general large in the lower troposphere as typically  $|(\partial_z u, \partial_z v)| < 10 \text{ m s}^{-1} \text{ km}^{-1}$  and  $N > 1 \cdot 10^{-2} \text{ s}^{-1}$ , that is,  $\text{Ri} > 1$ . Therefore, as discussed earlier, linear theory predicts well the filtering of TSIW in the lower troposphere via Scorer parameter trapping and critical level dissipation.

In the upper troposphere, in the absence of critical layers, an increase of the denominator  $(u - c)^2$  in Equation 1 can be interpreted as existing absolute wind shear  $|(\partial_z u, \partial_z v)|^2$ . Hence, the decrease of  $l^2$  is relatively well captured by  $\text{Ri}$  in this case, due to the relatively small contribution of the terms apart from  $N^2 \cdot (u - c)^{-2}$  in Equation 1 (Stephan, 2020). Note that  $\text{Ri}$  does not fully represent the effect of wind shear on wave trapping, as the sign of the wind shear relative to the direction of wave propagation is important. However, since we are unable to determine the wave phase velocity accurately,  $\text{Ri}$  is a useful proxy. Therefore, for upper-tropospheric wave reflection leading to an increased likelihood of TSIW trapping, both theories, linear and nonlinear, can be considered in terms of  $\text{Ri}$ , without assuming phase velocities of internal waves. Determining the phase velocity is difficult with the temporal resolution of the data used, especially for small scale waves such as those considered here.

This limitation in determining the phase velocity makes it challenging to identify the source of the waves. We considered whether mountains in South America could be the source of the waves detected over the eastern tropical Pacific, instead of our leading hypothesis that they are likely generated by convection. Our approach was to look at numerous additional representative cases, and to repeat our following analysis with eastern and western subdomains to determine whether the eastern domain has a higher occurrence of TSIW trapping. For the latter, we did not see such a pattern, nor did any of the cases suggest that these waves are generated by topography.

To study TSIW trapping in the real atmosphere, we need observations that provide corresponding wave signatures, which previous studies have done, for example, using true-color satellite imagery and searching for wave-like cloud patterns. In the absence of clouds, one can utilize water vapor-sensitive satellite imagery, that is, top of the atmosphere radiance measurements within wavelength bands that are mostly sensitive to the energy emitted by water vapor, approximately 6–7  $\mu\text{m}$  (Schmit et al., 2018). These water vapor bands “[...] sense the mean temperature of a variable-depth layer of moisture — a layer whose altitude and depth can vary, depending on both the temperature and moisture profile of the atmospheric column, as well as the satellite viewing angle” (Schmit et al., 2018).

Since TSIW trapping results in vertically coherent vertical velocity perturbations (Lane & Clark, 2002), signatures of TSIW trapping in water vapor-sensitive satellite imagery can be associated with local oscillations of brightness temperature perturbations as the waves locally modulate the vertical structure of temperature and humidity, that is, relative humidity. To the best of our knowledge, the two studies of Uhlenbrock et al. (2007) and Feltz et al. (2009) are the first to have examined water vapor bands in the context of tropospheric internal waves, focusing on mountain waves. In Lyapustin et al. (2014), mountain waves have been studied using a satellite-derived product of total column water vapor. In particular, the study Feltz et al. (2009) supports the connection between TSIW trapping and local oscillations of brightness temperature perturbations by comparing synthetic satellite imagery with high-resolution model data forced by a real-case mountain wave event. However, detecting these oscillations on spatial scales much larger than their typical wavelengths can be challenging because the corresponding perturbations are small compared to the overall brightness temperature variability (Wimmers et al., 2018). Building on the work of Feltz et al. (2009) and Wimmers et al. (2018), we here analyze imagery from the instrument Advanced Baseline Imager (ABI) on board the geostationary satellite GOES-16, whose nadir is on South America (75.2° W) and thus covers the eastern tropical Pacific, among other regions.

For an analysis over large temporal and spatial scales, it is crucial to be able to automatically detect TSIW trapping signatures in satellite imagery due to the volume of data. We are aware of only a few studies that address (semi)-automatic detection in this context: Wimmers et al. (2018) have applied high-pass filtering, that is, removing trends/frequencies in the brightness temperature field that are larger than the wavelengths of interest, to allow easier detection. However, they have not applied this method for a climatological study. Jann (2017) has proposed a method that uses an extended wavelet analysis that tests given angles and wavelengths, which can be a computationally expensive task depending on the number of angles, wavelengths and test locations. In Hindley et al. (2016) and Wright et al. (2017), internal waves in the stratosphere have been analyzed using a Stockwell transform method. A major advantage in analyzing stratospheric internal waves is their dominant imprint in satellite imagery, which is not the case for tropospheric ones.

We apply a local Fourier analysis to water vapor-sensitive satellite imagery to reveal the underlying frequencies. This not only allows us to measure local oscillations of brightness temperature perturbations, but also allows us to analyze all the available imagery more efficiently and still obtain qualitatively good results. One could also use established algorithms for pattern recognition from supervised machine learning. However, this involves a training phase where we lack well-studied training data. In this work, we take advantage of the simplicity of the pattern and detect it using a more direct method.

While we always use the term “trapping” throughout the remainder of this manuscript, our analysis does not exclude the possibility that we are measuring large amplitude waves that may not be trapped. However, the waves detected by our methods are most likely related to some form of trapping or wave filtering, and thus our term “trapping” is appropriate.

We have structured the manuscript as follows: We introduce the chosen data in Section 2 and explain how we process it in Section 3, along with an example case. In Section 4, we present the large scale environment of the reanalysis data as well as the distribution of TSIW trapping signatures. In addition, we address the intermittency of signatures on sub-seasonal scales. Finally, we conclude our results in Section 5.

## 2. Data

### 2.1. Water Vapor-Sensitive Satellite Imagery

We use water vapor-sensitive satellite imagery from the ABI on board the geostationary satellite GOES-16. Among the 16 bands of ABI, there are three bands at central wavelengths 6.2  $\mu\text{m}$ , 6.9  $\mu\text{m}$ , and 7.3  $\mu\text{m}$ , respectively, that are mostly sensitive to water vapor in the upper, middle, and lower troposphere, respectively (Schmit et al., 2017). Exemplary weighting functions can be found in Schmit et al. (2017, Figure 2). The satellite has been operating since the end of 2017 and the dataset is freely accessible at GOES-R Calibration Working Group and GOES-R Series Program (2017). We use all available data from 2018-01-01 to 2021-12-31, a period of exactly 4 years.

Except for a few negligible gaps, ABI creates “full disk” images every 10–15 min, with a resolution of about 2 km at the satellite’s nadir (75.2°W). As mentioned previously, this temporal resolution is insufficient to allow estimates of wave phase velocities for the scales of interest. An important issue we have to consider with ABI data is the satellite instrument measurement failures that result in longitudinal striping noise (Gunshor et al., 2020). These artifacts cause strong local shifts in the brightness temperature field that can be strongly misinterpreted depending on the analysis. In Section 3.1, we explain how we handle these artifacts.

### 2.2. Tropospheric Background State

For the tropospheric background state, we use the fifth generation reanalysis ERA5 by the European Centre for Medium-Range Weather Forecasts (Hersbach et al., 2020). ERA5 is, for example, freely accessible via the C3S Climate Data Store. We use the dataset of hourly profiles as a function of pressure levels  $P$  interpolated from its native model onto a horizontal grid with a resolution of 0.25° in longitude and latitude and a vertical resolution between 25 and 50 hPa in the altitude range of interest (Hersbach et al., 2018). While ERA5 is also available on model levels, providing a much denser vertical resolution, this dataset is provided horizontally on spherical harmonics, which need to be translated into geographic coordinates. Since we use multiple hourly variables over a period of 4 years, this dataset is not manageable in terms of both storage and computation time. We are particularly interested in the (squared) buoyancy frequency  $N^2$  and horizontal wind ( $u, v$ ). Since  $N^2$  is not provided by ERA5 directly, we calculate it via  $N^2 = g \cdot \left( T^{-1} \partial_z T - \frac{\gamma-1}{\gamma} P^{-1} \partial_z P \right)$ , where  $T$  is ERA5 temperature,  $\gamma = \frac{c_p}{c_v} = \frac{7}{5}$  the adiabatic index and the altitude  $z$  is inferred from ERA5 geopotential divided by  $g = 9.81 \text{ m s}^{-1}$ , the mean acceleration due to gravity. While we are computing the dry buoyancy frequency, it is known that moisture can have an impact on the buoyancy frequency (Durran & Klemp, 1982). We expect that this does not have a substantial impact on our findings, since we are focusing on clear-sky conditions in the upper troposphere.

### 2.3. Domain

One limiting factor in our analysis are medium/high-level clouds, which, like striping noise, cause strong local shifts in brightness temperature or simply obscure the scene in the troposphere. Figure 1 shows the spatial ERA5 low, medium, and high cloud cover mean, vertically separated at approximately 2 and 6 km with respect to the “standard atmosphere”, for the seasons DJF, MAM, JJA, and SON around the satellite’s nadir for our chosen time period. While ERA5 does not directly assimilate any cloud observations, it represents the monthly mean reasonably well (Yao et al., 2020). Since the water vapor bands peak above approximately 2 km, low clouds rarely influence the brightness temperatures. For medium and high clouds, we can see a clear separation between land and ocean, and over the tropical eastern Pacific, a separation between north and south of the equator. Hence, we chose to study the southern tropical eastern Pacific as shown in Figure 1. The domain was chosen primarily with regard to computational limits and the resolution of the satellite. Moreover, the domain is not subject to a clear seasonal cycle in medium/high-level cloud cover that might affect our conclusions. The satellite’s resolution median is approximately 2.2 km, with a maximum of 2.7 km.

## 3. Methods

Independently of the satellite imagery, we cluster daily mean profiles of ERA5 variables within the chosen domain and time period (Section 2) to characterize the large-scale environment and to identify periods when

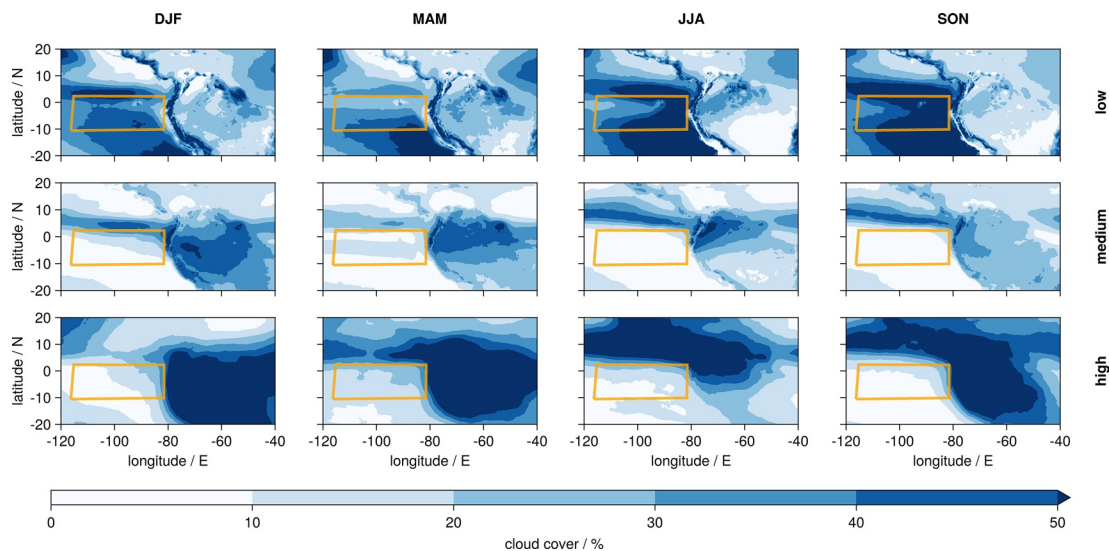


**Figure 1.** ERA5 low, medium, and high cloud cover mean from 2018-01-01 to 2021-12-31 separated into the seasons DJF, MAM, JJA, SON; the vertical separation is at approximately 2 and 6 km with respect to the “standard atmosphere”; our chosen domain is depicted in orange.

TSIW trapping is theoretically more likely. We use ERA5 profiles between 675 hPa ( $\sim 3.5$  km) and 162.5 hPa ( $\sim 13.7$  km). The vertical range was purposely chosen to be above the boundary layer and below the tropopause. Our clustering in horizontal space and time is based on applying a  $k$ -means algorithm to the horizontal wind. This algorithm computes  $k$  groups of profile positions and time points whose corresponding horizontal wind profiles are most “similar” to each other. We manually set  $k = 3$ , which is sufficient to separate the upper troposphere into clusters with distinct features that are robust to increasing  $k$ . The corresponding results are presented in Section 4.1, in particular Figure 4.

Together with the satellite imagery, we are able to link the hourly ERA5 profiles of horizontal wind and buoyancy frequency with a TSIW trapping measure. The TSIW trapping measure results from detecting TSIW trapping signatures in the available imagery using local Fourier analysis. We explain this method in more detail in Section 3.1 and present the corresponding results in Sections 4.2 and 4.3, where we first consider the TSIW trapping measure independently of ERA5 to summarize the large-scale distribution.

### 3.1. Detecting TSIW Trapping Signatures

We identify wave-like signals in brightness temperature based on three criteria: First, TSIW trapping signatures are local oscillations of brightness temperature. Second, these signature oscillations are small compared to the large-scale variability. Third, quasiperiodic patterns in an image result in a highly non-uniform frequency space of that image. Hence, our overall strategy consists of the following steps: (1) computing brightness temperature perturbations, (2) subdividing the domain into small overlapping “tiles”, (3) independently analyzing the spatial frequency space of each tile, (4) discarding tiles whose spatial frequency space is distorted and therefore not interpretable. Let us explain these steps in detail:

- (1) Instead of looking at the original brightness temperatures, we analyze their small-scale perturbations by applying a Gaussian filter on each satellite image, as proposed by Wimmers et al. (2018). The Gaussian filter convolves the brightness temperatures with a 2-dimensional Gaussian function of a specified standard deviation. The resulting smoothed brightness temperatures can be subtracted from the original brightness temperatures, to obtain the small-scale perturbations. The Gaussian filter's standard deviation is 2 pixels, which corresponds to approximately 5 km, and thus removes perturbations at wavelengths longer than typical TSIW.
- (2) We subdivide the satellite data, an equally-spaced 2-dimensional array of brightness temperature in the satellite's scan angles in  $x$ - and  $y$ -direction, with half-overlapping tiles that decompose the 2-dimensional space into a smaller “tile grid”. Each tile is a subarray of 64 pixels in  $x$  and  $y$ , a spatial length of about 60–80 km. Since TSIW in our domain have horizontal wavelengths of about 4–16 km, these tiles are small enough that TSIW dominate the tile and large enough that a sufficient number of oscillations is contained in order to classify them as waves.

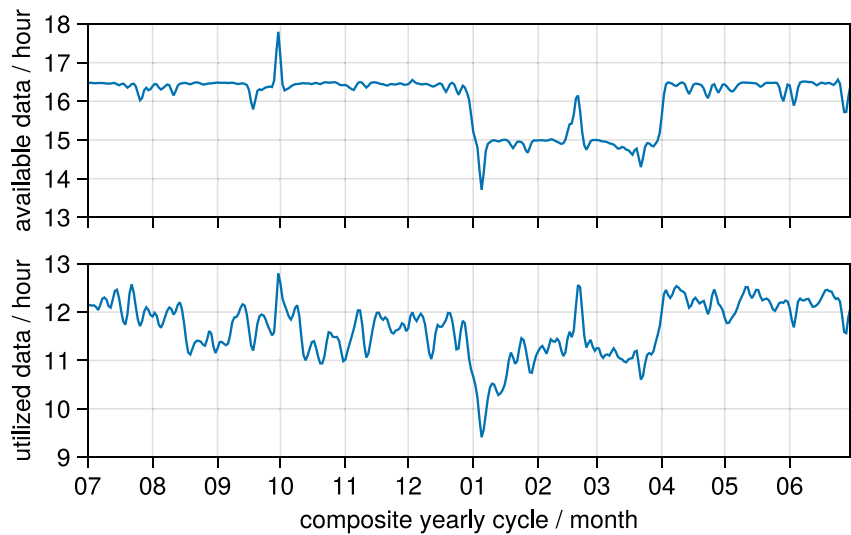


**Figure 2.** Smoothed daily mean of available and utilized satellite data.

(3) On each perturbation tile, we apply the 2-dimensional discrete Fourier transform, which transforms the original values in their spatial domain representation into the frequency domain representation given by complex values called Fourier coefficients. The Fourier coefficients encode the amplitude and phase of each 2-dimensional frequency. We are interested in the amplitudes, that is, the absolute values  $F$  of the Fourier coefficients. Quantifying the non-uniformity of  $F$  gives us a measure for TSIW trapping. Before that, we apply the following steps to  $F$  to minimize misinterpretations:

- Applying a high-pass filter to  $F$ , that is, ignoring small frequencies, in line with the expected TSIW wavelengths to minimize the influence of abruptly changing brightness temperatures, for example, associated with edges of clouds, which are not removed by the Gaussian filter.
- Replacing  $F$  with the absolute difference from the mean of  $F$  to minimize the impact of background noise, that is, a uniform distribution of frequencies, that could distort the signal of the overlying quasiperiodic pattern.

In Appendix A, we explain in detail how one can define a non-uniformity measure for the processed  $F$  values based on measuring the difference between probability distributions. The resulting TSIW trapping measure will be discussed in Section 3.2 using an example case and be applied to the entire data in Sections 4.2 and 4.3.

(4) In Section 2, we have already pointed out that abruptly changing brightness temperatures due to striping noise or medium/high clouds in the satellite data strongly affect the above analysis by distorting the frequency space. Therefore, we ignore tiles whose dominant frequency is 0 in  $x$ - or  $y$ -direction. The assumption is that natural wavy data rarely possess frequencies with perfect spatial alignment.

The fact that the waves commonly appear as quasiperiodic and quasi-2-dimensional facilitates this method. Using a Fourier analysis in (3), we naturally obtain the dominant wavelength and wave direction from the largest value of the processed  $F$  values. While the wavelength does not provide any new information, since we have optimized our method for a specific wavelength range, the wave angle is independent of our chosen scales and can be used as a sanity check when linking the TSIW trapping measure with ERA5. Based on the model studies of Balaji and Clark (1988) and Hauf and Clark (1989), one would expect the wave direction, that is, the direction perpendicular to the wave front, to become linearly correlated with the wind shear direction at a certain altitude for an increasing TSIW trapping measure threshold.

Figure 2 shows the daily mean of available and utilized satellite images per hour, smoothed by a Gaussian filter with a temporal standard deviation of 1 day to exclude unimportant anomalies. It is expected that a considerable amount of data is filtered using our criteria in (4), since in the absence of brightness temperature perturbations, a frequency of 0 is still likely. The shift in available data in January, February, and March is due to a change in the frequency of image production. Starting around April 2019, ABI has produced an image every 10 min ( $6 \cdot 3$  water vapor-sensitive satellite images per hour) instead of every 15 min ( $4 \cdot 3$  water vapor-sensitive satellite images per hour).

Since we only have hourly ERA5 profiles, we only use the hourly maximum of the TSIW trapping measure for each tile for our analyses in Section 4. This also addresses the small seasonal biases in available and utilized satellite data (Figure 2), since we do not expect that the differences in hourly satellite data will strongly affect the hourly maximum. We link each hourly ERA5 profile with its closest tile grid position and consider the maximum of the TSIW trapping measure within the following hour.

### 3.2. Example Case

Before presenting the results for the entire chosen time period and domain, we look at two different sub-regions of the domain in detail, on a day with one of the largest TSIW trapping occurrences. The two scenes, A and B, are depicted in Figure 3 (A: a–g, B: h–n) and have been selected according to the clear distinction in TSIW trapping signatures.

In contrast to scene B, scene A has strong signatures in the water vapor-sensitive image, ABI's "upper-level water vapor" band at a wave length of about 6.2  $\mu\text{m}$ . There are also clear imprints on the boundary layer clouds for scene A in ABI's "clean longwave window" band at a wavelength of about 10.3  $\mu\text{m}$ , a band where one is able to clearly see boundary layer clouds in the absence of high-level clouds.

Figures 3c and 3j each show an example tile whose position is indicated in Figures 3b and 3i, respectively, along with the normalized frequency space in Figures 3d and 3k, respectively. While scene A's frequencies are concentrated around approximately 0.2  $\text{pixel}^{-1}$ , which corresponds to a wavelength of about 9 km, B's frequencies are relatively uniformly distributed, resulting in a smaller TSIW trapping measure value (see Figures 3e and 3l). Based on experiments, a good TSIW trapping measure threshold is between 0.08 and 0.10, as can be clearly seen in Figures 3e and 3l, for example.

Our TSIW trapping measure is only one possible approach to an automated analysis of TSIW trapping signatures. While we have carefully optimized this measure to capture TSIW signatures as well as possible, in the wavelength range of interest, there are of course other processes that can induce a locally wavy brightness temperature field, as already discussed in Jann (2017). Our approach has been to iteratively improve the measure with different cases, while manually sanity checking the results with cloud imprints in true-color satellite imagery.

It should be noted that clear signatures can and do occur in the absence of shallow clouds, which one might not infer from our example case. This is not the purpose of the chosen scenes. We want to emphasize that while we have a clear distinction between the two regions in terms of our TSIW trapping measure, this is not the case for the mean ERA5 buoyancy frequency and horizontal wind for each scene shown in Figures 3f and 3g, 3m and 3n. As there are only subtle differences in the profiles, in this case the chosen ERA5 profiles alone cannot explain why we see clear signatures in Scene A compared to Scene B. However, this does not rule out a statistical relationship in general. For both scenes, based on the theory discussed in Section 1, it is likely that the westerly wind shear in the lower troposphere filters TSIW by trapping smaller wavelengths, while the strong easterly wind shear combined with a small buoyancy frequency in the upper troposphere creates a nonlinear reflection layer. Both processes increase the likelihood for upper-tropospheric TSIW trapping.

The main point of this example case is that it is difficult to explain individual TSIW trapping occurrences with the available data, and therefore we must rely on statistical relationships linking these occurrences to background variables. A detailed quantitative analysis would require knowledge that is not available. In general, for example, it is unclear whether a weaker signature is actually due to a smaller wave amplitude or rather the result of the satellite's resolution or viewing angle, or the large scale variability in temperature and moisture that affect the brightness temperature field. Since TSIW signatures are barely resolved in ABI imagery, certain wavelengths are simply better detected by ABI, as pointed out in Jann (2017, Figure 5). Regarding the ERA5 data, we expect it to be smoother than reality, possibly with local biases due to limitations in data assimilation. We therefore focus on the statistical relationship between TSIW and ERA5 over the entire domain and do not attempt to explain local events.

## 4. Results

In Sections 4.1 and 4.2, we look at the large-scale distribution of the background state and the TSIW trapping signatures, respectively. We analyze their joint distribution in Section 4.3, to derive our main result, summarized in Figure 10.

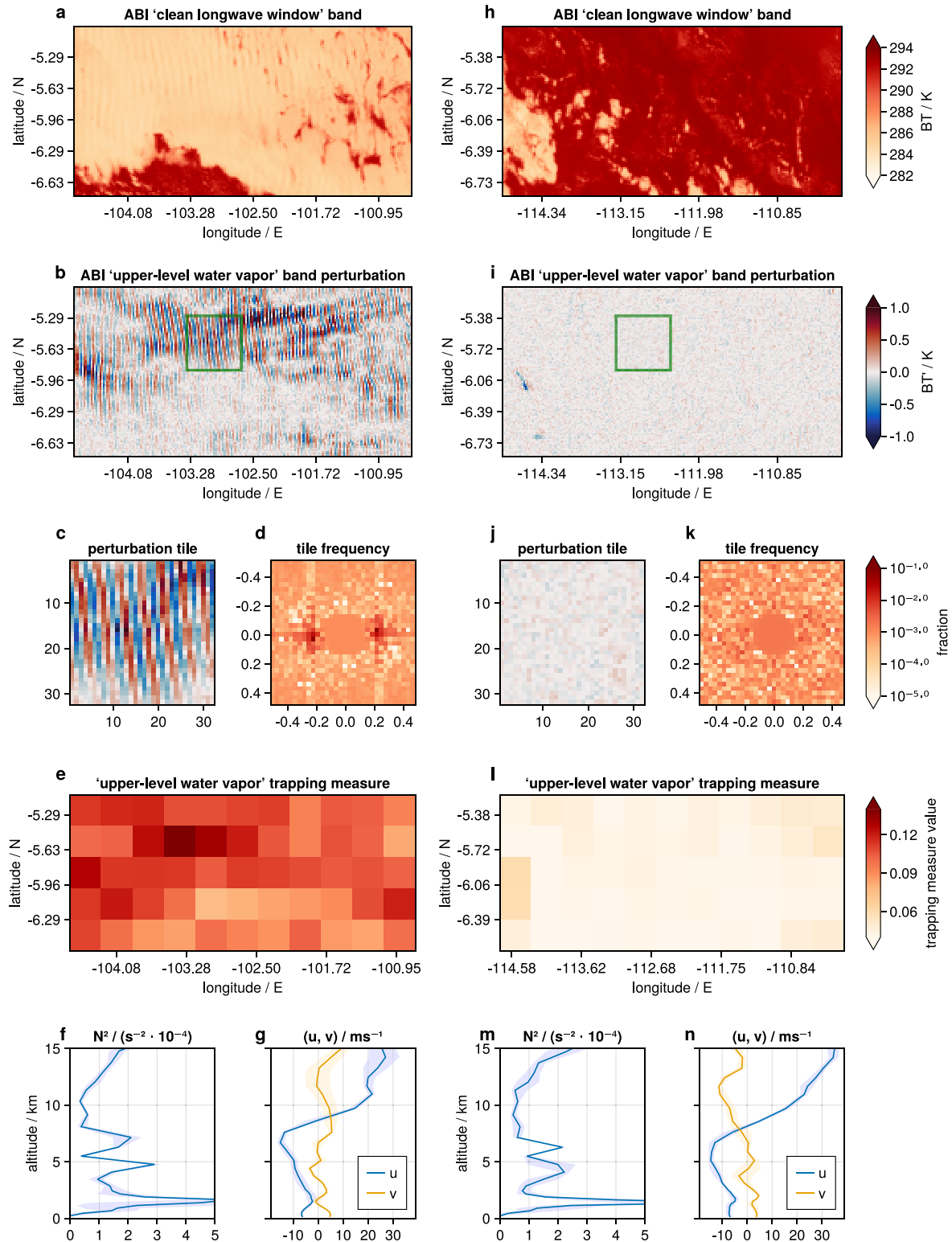


**Figure 3.** Example case of two different sub-regions a–g/h–n on December 23, 03:00 (UTC); a/h: brightness temperatures of ABI’s “clean longwave window” band; b/i: brightness temperature perturbations of ABI’s “upper-level water vapor” band; c–d/j–k: example tile with its normalized processed absolute Fourier coefficients (see Section 3.1), tile position is indicated in b/i, depicted coordinates are pixels and pixel frequencies, respectively; e/l: TSIW trapping measure for each tile (see Section 3.1); f–g/m–n: mean ERA5 profiles of  $N^2$ ,  $u$ , and  $v$  with min/max-bands; a/h, b/i, e/l have actually coordinates in the satellite’s scan angle, but have been converted to approximate geographic coordinates for better readability.

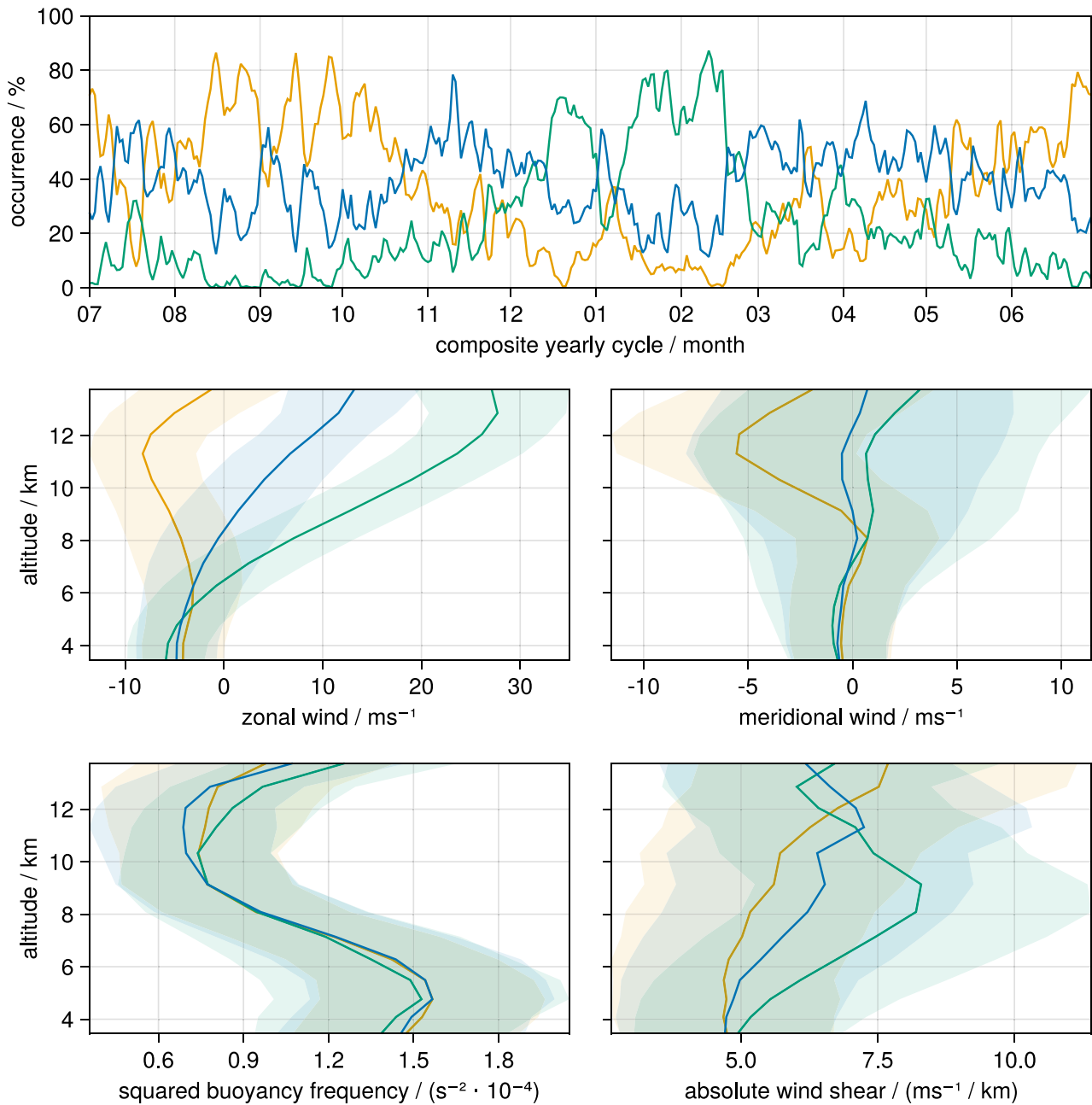


**Figure 4.** Clustering of daily mean ERA5 profiles between 675 hPa and 162.5 hPa within our chosen period and domain (Section 2); the clustering is based on a ( $k = 3$ )-means clustering applied to the horizontal wind (Section 3); the first plot shows the relative dominance of each cluster throughout the year; the remaining plots show for each respective variable the cluster mean with a standard deviation band.

#### 4.1. Large-Scale Environment

As discussed in Section 3, we analyze the large-scale distribution of the background state by clustering ERA5 profiles, specifically by applying a ( $k = 3$ )-means clustering to the horizontal wind. The resulting clustering is given in Figure 4, which shows the temporal relative distribution as well as the mean profiles of horizontal wind, squared buoyancy frequency, and absolute wind shear for each of the three clusters. The standard deviation bands around the cluster mean profiles help to understand at which altitude levels the clustering has resulted in well-defined features and at which there is too much variance. However, since the general scaling of absolute wind speed is larger in the upper troposphere than in the middle troposphere, the  $k$ -means algorithm is more sensitive to the upper troposphere as all levels are treated equally.

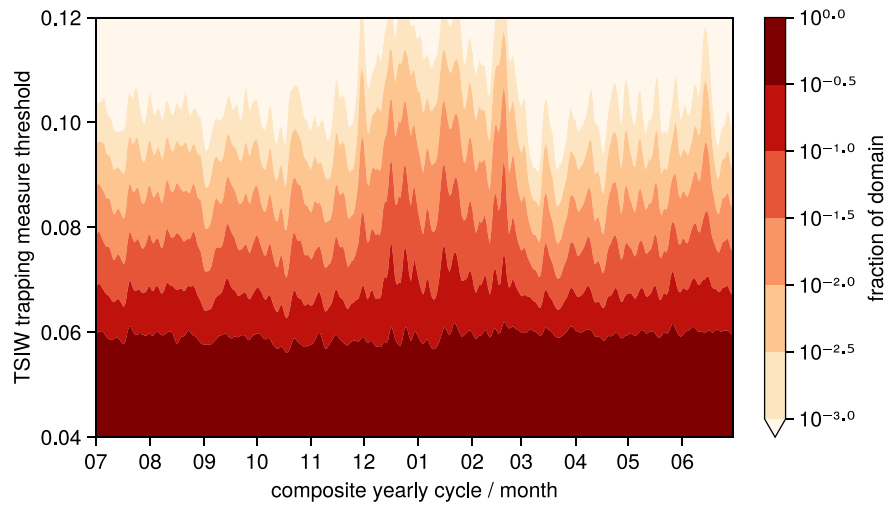


**Figure 5.** Smoothed daily spatial coverage of TSIW trapping signatures.

The upper-tropospheric horizontal wind exhibits distinct regimes, while the upper-tropospheric buoyancy frequency is relatively invariant throughout the year. Applying  $k$ -means only to the buoyancy frequency shows that its variability is not subject to any seasonal cycle, which can already be expected from Figure 4. Therefore, the large-scale variability of the Richardson number reduces to the absolute wind shear, which in contrast is subject to a clear seasonal cycle.

During DJF, our domain is dominated by upper-tropospheric easterly jets, with a distinct peak in each month, as confirmed by the temporal distribution in Figure 4 (green cluster). During the rest of the year, the horizontal wind is relatively weak and has no clear direction, which also results in weaker absolute wind shear. Irrespective of the number of clusters, the domain primarily separates into two regimes, DJF and the rest of the year. This leads to two important observations: First, small values of  $Ri$  are more likely in the upper troposphere throughout the year due to  $N$  decreasing vertically. Second, small values of  $Ri$  in the upper troposphere are more likely in DJF due to an intermittent increase in  $|\partial_z u, \partial_z v|$ .

#### 4.2. Large-Scale Trapping

As described in Section 3.1, for each available satellite image within the chosen domain, we compute our TSIW trapping measure along the defined tile grid, skipping tiles that do not meet our criteria. Calculating the daily mean fraction of tiles that exceed a certain TSIW trapping threshold results in Figure 5. The daily mean was smoothed using a Gaussian filter with a temporal standard deviation of 1 day to exclude unimportant anomalies. Signatures become visibly notable for values larger than 0.06–0.08, and a clear signature can be assumed at values larger than 0.08–0.10, as discussed in Section 3.2. With an increasing TSIW trapping measure threshold, we see a clear trend of increased signature coverage during DJF, as expected by the results in Section 4.1. Moreover, we also see the distinct peaks in each month we noticed for the horizontal wind.

Our domain has a size of approximately  $10^7$  km<sup>2</sup>. The temporal variability for thresholds between 0.04 and 0.06 is primarily due to missing satellite images or our tile filtering (see Figure 2). The number of signature occurrences decreases exponentially with an increasing threshold, but for a threshold of 0.10, we still have days when at least 1% of the domain is covered. Besides the limitations discussed in Section 3.2, the scarcity of TSIW trapping signatures is another limiting factor in the analysis that we aim to address with enough data. It is unclear to what extent Figure 5 reflects the true frequency of TSIW trapping in our domain, but a seasonal bias due to data filtering (Figure 2) or due to medium/high-level clouds (Figure 1) is unlikely. Furthermore, the clear correlation between the horizontal wind and TSIW trapping signatures during DJF gives us confidence in our detection method.

The distribution of TSIW trapping signatures is subject to daily variability, and we could not detect a diurnal cycle. The signature distribution consists of sparse short periods, in the order of 1–2 days, of large-scale signature

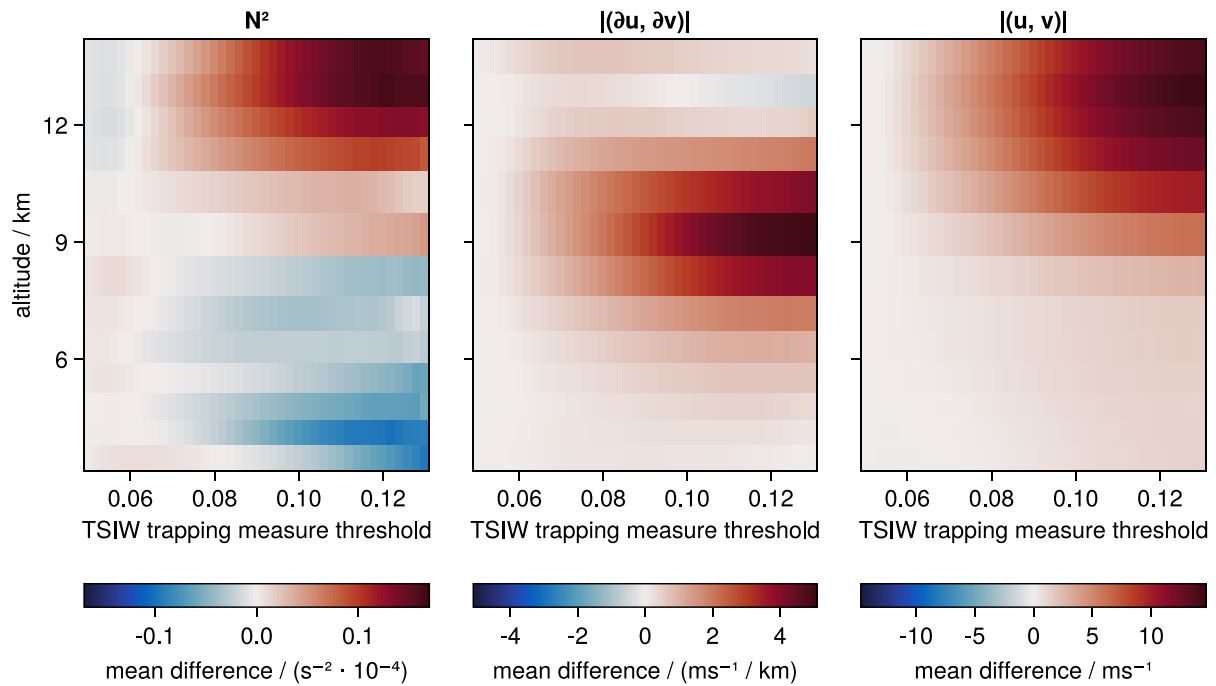


**Figure 6.** The mean difference  $\text{mean}(\mathcal{P}_{>\epsilon}) - \text{mean}(\mathcal{P}_{\leq\epsilon})$ , as defined in Section 4.3, with respect to a TSIW trapping measure threshold  $\epsilon$ , for squared buoyancy frequency  $N^2$ , absolute wind shear  $|(\partial_z u, \partial_z v)|$  and wind speed  $|(u, v)|$  along ERA5 pressure levels.

coverage up to 10% for thresholds between 0.08 and 0.10, rather than consistent signature occurrences with a smaller coverage on longer time scales. With ERA5, we were not able to explain variability on shorter periods than 2 days or smaller domains. In Section 4.3, we address the sub-seasonal variability and the associated relation between an increased upper-tropospheric wind shear and an increased likelihood of TSIW trapping.

### 4.3. Sub-Seasonal Variability

We have seen in Sections 4.1 and 4.2 that during DJF, the increased upper-tropospheric wind shear increases the likelihood of large-scale upper-tropospheric TSIW trapping in contrast to the rest of the year. In this section, we address the reason of increased likelihood on sub-seasonal time scales. We have already seen in Section 4.2 that there is daily variability in TSIW trapping, and ask if this can be attributed to an intermittent upper-tropospheric wind shear.

To address correlations beyond large-scale trends, we have linked each hourly ERA5 profile with its closest tile grid position, as explained in Section 3.1. To reduce the dimensionality of the data, we first investigate at which altitude levels horizontal wind and buoyancy frequency change with respect to an increasing TSIW trapping measure threshold, that is, we are interested in how the distributions of these variables deviate from the remaining set of ERA5 profiles: For a given trapping measure threshold  $\epsilon$ , we can divide the set of all ERA5 profiles into profiles  $\mathcal{P}_{>\epsilon}$  whose corresponding TSIW trapping measure value exceeds  $\epsilon$  and into profiles  $\mathcal{P}_{\leq\epsilon}$  whose do not. Let  $\text{mean}(\mathcal{P}_{>\epsilon})$  and  $\text{mean}(\mathcal{P}_{\leq\epsilon})$  denote the mean as a function of ERA5 pressure levels. Then, for each  $\epsilon$ , we can compute the mean difference  $\text{mean}(\mathcal{P}_{>\epsilon}) - \text{mean}(\mathcal{P}_{\leq\epsilon})$  as a function of ERA5 pressure levels.

In Figure 6, we show the resulting 2-dimensional mean difference for  $N^2$ ,  $|(\partial_z u, \partial_z v)|$  and  $|(u, v)|$ . While the mean difference of  $N^2$ ,  $|(\partial_z u, \partial_z v)|$  and  $|(u, v)|$  change with an increasing threshold  $\epsilon$ , the change in  $|(\partial_z u, \partial_z v)|$  and  $|(u, v)|$ , is much stronger with respect to the standard deviation  $\text{std}(\mathcal{P}_{>\epsilon})$  along the ERA5 pressure levels, shown in Figure 7 analogous to Figure 6. This indicates that the horizontal wind is much more sensitive to our TSIW trapping measure than the buoyancy frequency. However, this is most likely due to a steady buoyancy frequency throughout the year, as seen in Section 4.1. The mean difference of absolute wind shear peaks at an ERA5 pressure level of 325 hPa, an altitude of about 9 km.

In Figure 8, we show the mean and standard deviation of  $N^2$ ,  $|(\partial_z u, \partial_z v)|$ , and  $|(u, v)|$  for  $\mathcal{P}_{>\epsilon}$  at three different ERA5 pressure levels, including 325 hPa. There is a clear shift with an increasing TSIW trapping threshold for

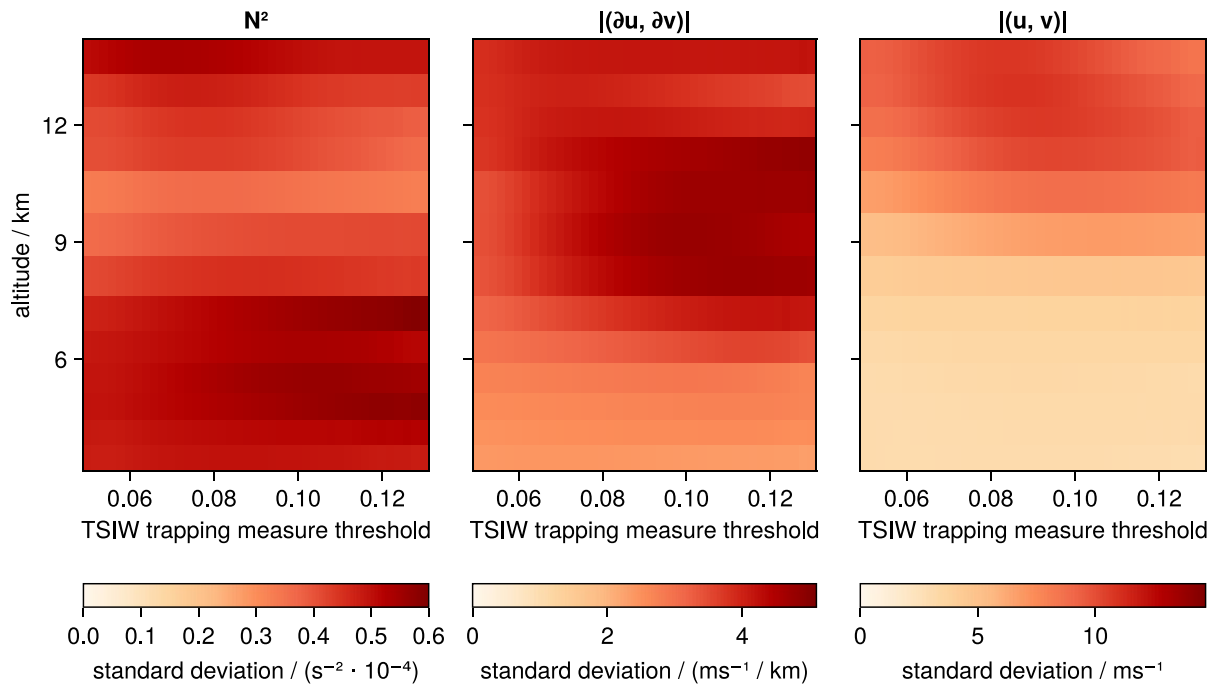


**Figure 7.** Standard deviation of  $\mathcal{P}_{>\epsilon}$ , as defined in Section 4.3, with respect to a TSIW trapping measure threshold  $\epsilon$  for squared buoyancy frequency  $N^2$ , absolute wind shear  $|(\partial_z u, \partial_z v)|$  and wind speed  $|(u, v)|$  along ERA5 pressure levels.

the mean of absolute wind shear at 325 hPa and of wind speed at 212.5 hPa in contrast to the buoyancy frequency. Moreover, at these ERA5 pressure levels we see a clear separation between the wind distributions at a TSIW trapping threshold of about 0.08, supporting our statement that a clear TSIW signature can be assumed above 0.08 – 0.10. One should keep in mind that the number of signature occurrences decreases exponentially with an increasing TSIW trapping threshold, as seen in Figure 5, resulting in more uncertain distributions. The peak at 325 hPa is supported by the relationship between the angle of absolute wind shear and the TSIW trapping signature angle with respect to a threshold of 0.09, derived from the Fourier analysis as described in Section 3.1. In Figure 9, we show this relationship at the same ERA5 pressure levels as in Figure 8. At 325 hPa, there is a clear change toward an expected linear relationship, as discussed in Section 3.1 (4).

Based on the previous distribution analysis, we look at the median buoyancy frequency  $N$ , absolute wind shear  $|(\partial_z u, \partial_z v)|$ , and therefore also the Richardson number  $Ri$  at an ERA5 pressure level of 325 hPa. Since it cannot be assumed that  $Ri$  is normally distributed, we show in Figure 10 the median surrounded by an interquartile range band for  $N$ ,  $|(\partial_z u, \partial_z v)|$  and  $Ri$  with respect to our TSIW trapping measure during DJF and the rest of the year ( $\neg DJF$ ). As already noted,  $N$  is not changing with an increasing TSIW trapping threshold. In contrast, even though there is a large variability,  $|(\partial_z u, \partial_z v)|$  has a clear positive relationship with an increasing TSIW trapping threshold. Therefore, the clear negative relationship of  $Ri$  with an increasing TSIW trapping threshold is primarily due to  $|(\partial_z u, \partial_z v)|$ . However, as seen in Section 4.1, the minor influence of  $N$  is due to its steady nature in the upper troposphere throughout the year. The sub-seasonal relationship of absolute wind shear with TSIW trapping is more evident during DJF than the rest of the year.

## 5. Conclusion and Discussion

We developed a measure for TSIW trapping signatures in water vapor-sensitive satellite imagery, based on a local Fourier analysis of brightness temperature perturbations. This allows us to analyze 4 years of water vapor-sensitive satellite imagery from ABI on board GOES-16 within a domain size of about  $10^7 km^2$  over the eastern tropical Pacific. By linking the TSIW trapping measure with ERA5 data, we are able to infer based on theory that sub-seasonal intermittent upper-tropospheric absolute wind shear increases the likelihood of TSIW trapping in the real atmosphere. While idealized simulations and observational case studies already support this statement, our work is the first step toward a systematic analysis of the real atmosphere on larger scales. Furthermore, the increased wind shear results in a small

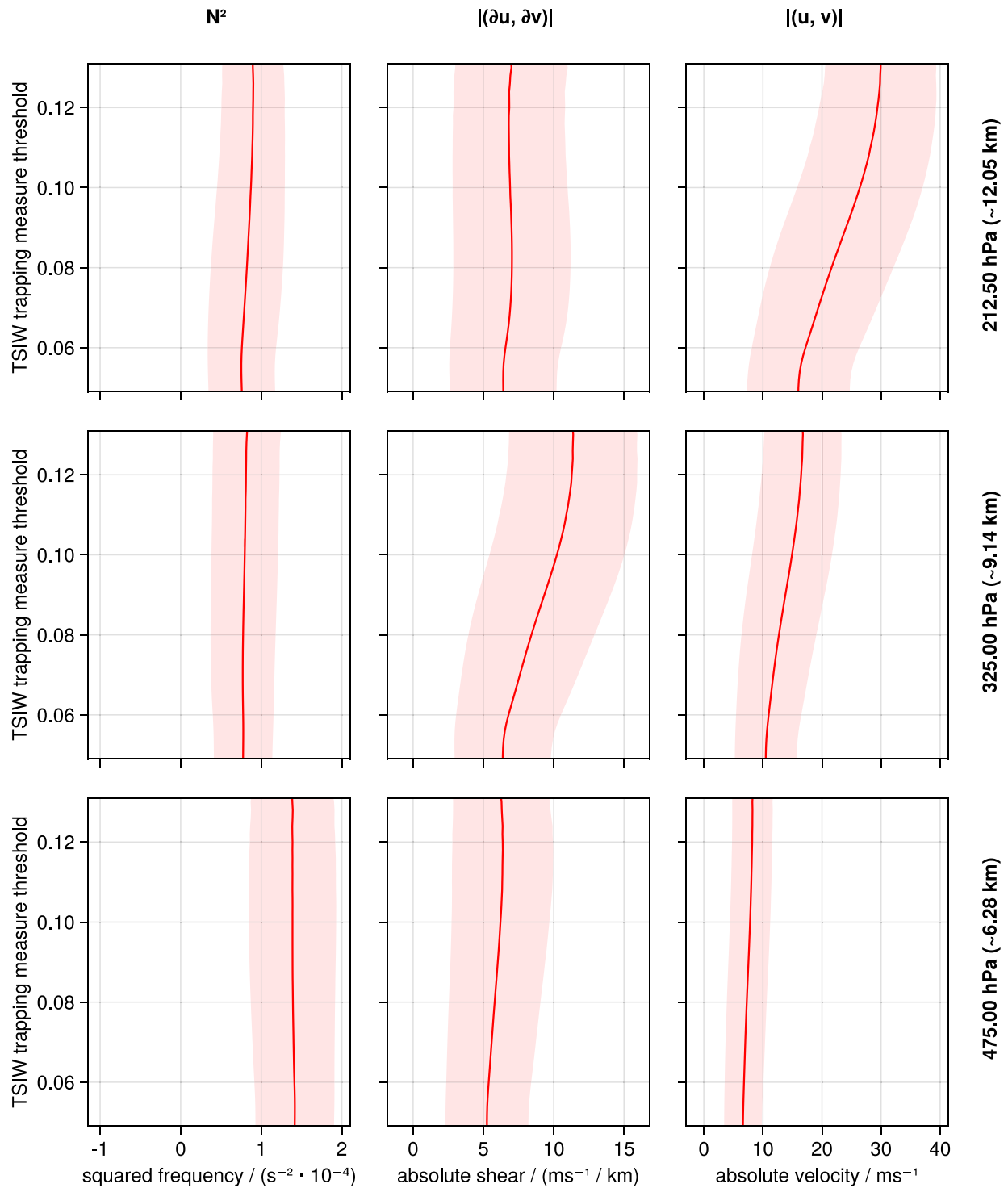


**Figure 8.** The mean with a standard deviation band of  $\mathcal{P}_{>\epsilon}$ , as defined in Section 4.3, with respect to a TSIW trapping measure threshold  $\epsilon$  for squared buoyancy frequency  $N^2$ , absolute wind shear  $|(\partial_z u, \partial_z v)|$  and wind speed  $|(\mathbf{u}, \mathbf{v})|$  at different ERA5 pressure levels.

Richardson number due to a steady small buoyancy frequency. However, the suitability of the Richardson number in predicting the likelihood of TSIW trapping requires further analysis in regions where the buoyancy frequency varies.

A key limitation in our analysis is the uncertainty arising from the detection of TSIW trapping signatures in satellite imagery. These signatures are not yet well understood in quantitative terms. Most importantly, we lack

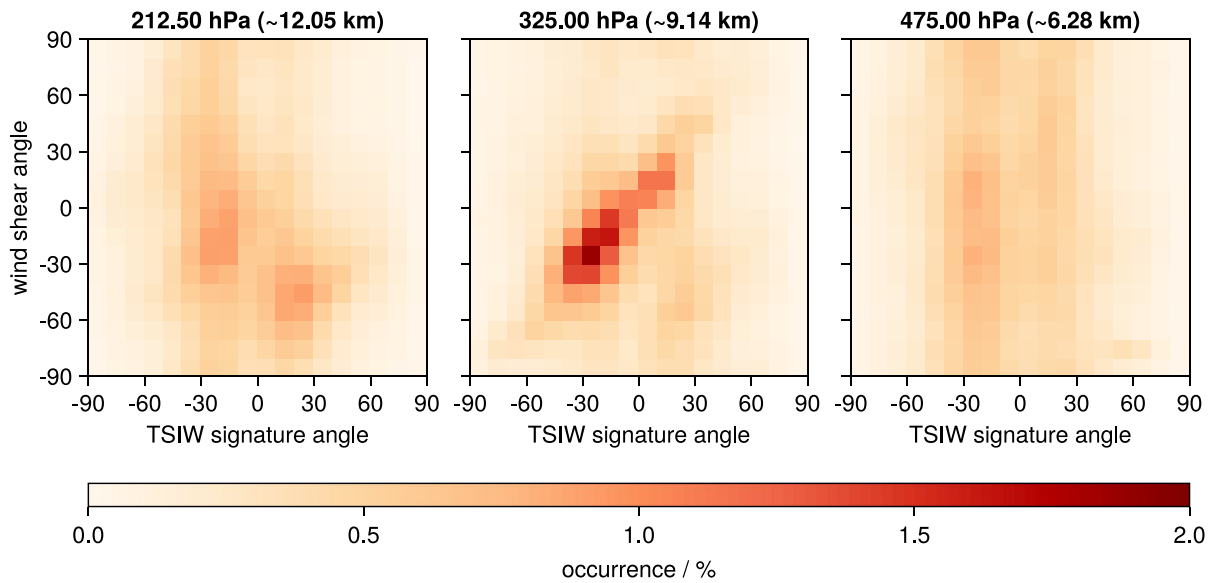


**Figure 9.** Relation between the direction of TSIW signatures and the direction of wind shear at multiple ERA5 pressure levels; the TSIW trapping measure threshold is 0.09 and the direction of the resulting signatures is perpendicular to the strongest wave front; an angle of  $0^\circ$  encodes the zonal direction, positive angles encode directions turning anticlockwise and negative angles clockwise.

a good training set with which we could objectively compare detection methods and evaluate their strengths and weaknesses. In this context, there are a number of open questions: (a) Is it possible to utilize the amplitudes of the brightness temperature perturbations to infer the strength of TSIW? (b) Is it possible to determine the vertical extent of TSIW by combining different overlapping water vapor bands? (c) Is it possible to determine the phase velocity of TSIW by considering successive satellite images with enhanced spatiotemporal resolution? (d) How sensitive is the detection of TSIW trapping signatures to the satellite's resolution or viewing angle? One approach to address (a) and (b) is to extend the study in Feltz et al. (2009), that is, studying synthetic satellite images computed from model simulations.

This analysis was possible primarily due to the improved resolution of ABI on board GOES-16 compared to imagers on board previous GOES satellites (Feltz et al., 2009). The Advanced Himawari Imager (AHI) on board Himawari 8, a geostationary satellite at  $140.7^\circ\text{E}$  (nadir), has similar specifications to ABI (BESSHO et al., 2016). In particular, AHI also provides three water vapor-sensitive bands at the same central wavelengths as ABI with

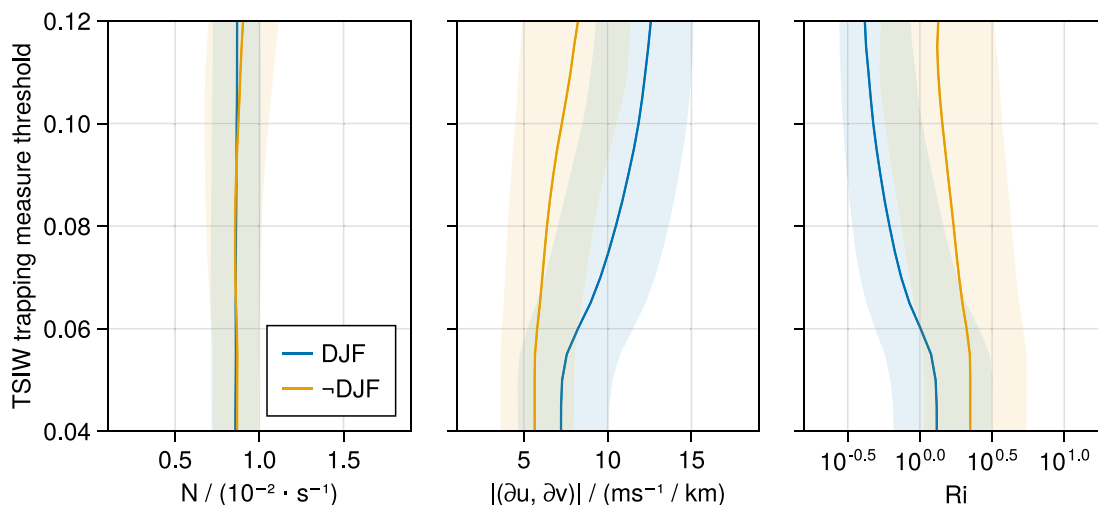


**Figure 10.** Median with interquartile range bands of  $P_{>\epsilon}$ , as defined in Section 4.3, with respect to a TSIW trapping measure threshold  $\epsilon$  for buoyancy frequency  $N$ , absolute wind shear  $|(\partial_z u, \partial_z v)|$ , and Richardson number  $Ri$  at 325 hPa ( $\sim 9.14$  km) during DJF and the rest of the year ( $\neg DJF$ ).

the same resolution of 2 km at the satellite's nadir. AHI covers the Western Pacific, among other regions, and is therefore suitable for a similar study.

On the other hand, since our method can be used to identify periods and regions with a high rate of trapping signatures in satellite imagery, it could be a useful tool to identify other measurements from field campaigns or observation stations that may have recorded such events. In particular, radiosondes could provide a more realistic background state to help understand the observed signatures (Lane et al., 2003). Furthermore, the integration of such detection methods into nowcasting systems has already been discussed in Jann (2017).

## Appendix A: Measuring the Non-Uniformity of a Frequency Space

Given a local 2-dimensional brightness temperature perturbation (see Figure 3), that is, a 2-dimensional finite array of equally-spaced samples, we can apply the 2-dimensional discrete Fourier transform to obtain the frequency domain representation given by complex values called Fourier coefficients (see Section 3.1). Since we want to know if the local brightness temperature perturbation is dominated by only a few frequencies, we want to quantify how non-uniform the amplitudes of the 2-dimensional frequencies are, that is, measure the non-uniformity of the absolute values  $F$  of the Fourier coefficients.  $F$  can be interpreted as a distribution over the finite state space  $\mathcal{Y}$  of all 2-dimensional Fourier frequencies and can be assumed to be normalized, that is,  $\sum_{Y \in \mathcal{Y}} F(Y) = 1$ . We are now interested in how much the normalized distribution  $F$  diverges from a uniform distribution  $U(Y) = |\mathcal{Y}|^{-1}$ , that is, the situation where each 2-dimensional frequency contributes equally to the local brightness temperature perturbation.

Whether a certain model distribution  $P$  resembles the real distribution  $Q$  over a finite state space  $\mathcal{Y}$ , is a common question in data science. One option is to compute well-studied  $f$ -divergences  $D_f(P||Q) := \sum_{Y \in \mathcal{Y}} f\left(\frac{P(Y)}{Q(Y)}\right) \cdot Q(Y)$  (Sason & Verdú, 2016), to measure the deviation of  $P$  from  $Q$ . This requires the reasonable assumption that  $P$  is “absolutely continuous” with respect to  $Q$ , abbreviated  $P \ll Q$  and defined by  $Q(Y) = 0 \Rightarrow P(Y) = 0$ , that is, if a state is impossible under  $Q$ , then the same should hold for  $P$ . In the other case, it is easily justifiable to reject  $P$ . Since in our case  $U = Q$  is never zero, by definition we have  $F \ll U$ .

We use the Kullback–Leibler divergence  $D_{KL}(P||Q)$ , also known as relative entropy, an  $f$ -divergence defined by the generator  $f(x) = x \log(x)$ , that is,  $D_{KL}(P||Q) = \sum_{Y \in \mathcal{Y}} P(Y) \cdot \log \frac{P(Y)}{Q(Y)}$ . Another  $f$ -divergence could be the total variation distance  $D_{|x-1|}(P||Q) = \sum_{Y \in \mathcal{Y}} |P(Y) - Q(Y)|$ , which might be more intuitive. But, due to Pinsker's inequality  $\log(e) \cdot (D_{|x-1|}(P||Q))^2 \leq 2 \cdot D_{KL}(P||Q)$  (Sason & Verdú, 2016),  $D_{KL}(P||Q)$  is at least as sensitive as  $D_{|x-1|}(P||Q)$  if  $P$  differs from  $Q$ .

In our case, the Kullback–Leibler divergence simplifies to  $D_{KL}(F||U) = \sum_{Y \in \mathcal{Y}} F(Y) \cdot \log F(Y) + \log |\mathcal{Y}| = \log |\mathcal{Y}| - H(F)$ , where  $H(P) = -\sum_{Y \in \mathcal{Y}} P(Y) \cdot \log P(Y)$  is the entropy of a distribution  $P$  over a finite state space  $\mathcal{Y}$ . Taking the logarithm with respect to the base  $|\mathcal{Y}|$  gives  $D_{KL}(F||U) = 1 - H(F)$ . Thus we are essentially interested in the entropy of  $F$ . For a local brightness temperature perturbation, this entropy gives us a measure of the non-uniformity of the respective frequency space. This measure allows us to identify wave-like signals in a brightness temperature field by choosing a threshold that this measure must exceed.

## Data Availability Statement

The NOAA GOES-R Series Advanced Baseline Imager (ABI) Level 1b Radiances providing the water vapor-sensitive satellite imagery from ABI on board the geostationary satellite GOES-16 are available at GOES-R Calibration Working Group and GOES-R Series Program (2017). The dataset of hourly profiles on pressure levels of the fifth generation reanalysis ERA5 by the European Centre for Medium-Range Weather Forecasts is accessible via the C3S Climate Data Store (Hersbach et al., 2018).

## References

- Balaji, V., & Clark, T. L. (1988). Scale selection in locally forced convective fields and the initiation of deep cumulus. *Journal of the Atmospheric Sciences*, 45(21), 3188–3211. [https://doi.org/10.1175/1520-0469\(1988\)045<3188:ssilfc>2.0.co;2](https://doi.org/10.1175/1520-0469(1988)045<3188:ssilfc>2.0.co;2)
- Balaji, V., Redelsperger, J.-L., & Klaassen, G. P. (1993). Mechanisms for the mesoscale organization of tropical cloud clusters in GATE phase III. Part I. Shallow cloud bands. *Journal of the Atmospheric Sciences*, 50(21), 3571–3589. [https://doi.org/10.1175/1520-0469\(1993\)050<3571:mftmoo>2.0.co;2](https://doi.org/10.1175/1520-0469(1993)050<3571:mftmoo>2.0.co;2)
- Bessho, K., Date, K., Hayashi, M., Ikeda, A., Imai, T., Inoue, H., et al. (2016). An introduction to Himawari-8/9 – Japan's new-generation geostationary meteorological satellites. *Journal of the Meteorological Society of Japan Series II*, 94(2), 151–183. <https://doi.org/10.2151/jmsj.2016-009>

## Acknowledgments

This work was supported by the ARC Centre of Excellence for Climate Extremes (CE170100023). R. Vicari acknowledges support by the Melbourne Research Scholarship. R. Vicari is grateful to Radomyra Shevchenko for her feedback on an earlier version of the manuscript, which improved the methodology and presentation. Open access publishing facilitated by The University of Melbourne, as part of the Wiley - The University of Melbourne agreement via the Council of Australian University Librarians.

- Böhme, T., Hauf, T., & Lehmann, V. (2004). Investigation of short-period gravity waves with the Lindenberg 482 MHz tropospheric wind profiler. *Quarterly Journal of the Royal Meteorological Society*, *130*(603), 2933–2952. <https://doi.org/10.1256/qj.03.179>
- Böhme, T., Lane, T. P., Hall, W. D., & Hauf, T. (2007). Gravity waves above a convective boundary layer: A comparison between wind-profiler observations and numerical simulations. *Quarterly Journal of the Royal Meteorological Society*, *133*(625), 1041–1055. <https://doi.org/10.1002/qj.72>
- Clark, T. L., Hauf, T., & Kuettner, J. P. (1986). Convectively forced internal gravity waves: Results from two-dimensional numerical experiments. *Quarterly Journal of the Royal Meteorological Society*, *112*(474), 899–925. <https://doi.org/10.1002/qj.49711247402>
- Dinh, T., Podglajen, A., Hertzog, A., Legras, B., & Plougonven, R. (2016). Effect of gravity wave temperature fluctuations on homogeneous ice nucleation in the tropical tropopause layer. *Atmospheric Chemistry and Physics*, *16*(1), 35–46. <https://doi.org/10.5194/acp-16-35-2016>
- Durran, D. R., & Klemp, J. B. (1982). On the effects of moisture on the Brunt-Väisälä frequency. *Journal of the Atmospheric Sciences*, *39*(10), 2152–2158. [https://doi.org/10.1175/1520-0469\(1982\)039<2152:oteomo>2.0.co;2](https://doi.org/10.1175/1520-0469(1982)039<2152:oteomo>2.0.co;2)
- Feltz, W. F., Bedka, K. M., Otkin, J. A., Greenwald, T., & Ackerman, S. A. (2009). Understanding satellite-observed mountain-wave signatures using high-resolution numerical model data. *Weather and Forecasting*, *24*(1), 76–86. <https://doi.org/10.1175/2008WAF2222127.1>
- Gibert, F., Arnault, N., Cuesta, J., Plougonven, R., & Flamant, P. H. (2011). Internal gravity waves convectively forced in the atmospheric residual layer during the morning transition. *Quarterly Journal of the Royal Meteorological Society*, *137*(659), 1610–1624. <https://doi.org/10.1002/qj.836>
- GOES-R Calibration Working Group and GOES-R Series Program. (2017). NOAA GOES-R series advanced baseline imager (ABI) level 1b radiances [Dataset]. NOAA National Centers for Environmental Information. <https://doi.org/10.7289/V5BV7DSR>. Accessed 2022
- Gunshor, M. M., Schmit, T. J., Pogorzala, D. R., Lindstrom, S. S., & Nelson, J. P. (2020). GOES-R series ABI imagery artifacts. *Journal of Applied Remote Sensing*, *14*(3), 1–19. <https://doi.org/10.1117/1.JRS.14.032411>
- Hauf, T. (1993). Aircraft observation of convection waves over southern Germany—A case study. *Monthly Weather Review*, *121*(12), 3282–3290. [https://doi.org/10.1175/1520-0493\(1993\)121<3282:aocowo>2.0.co;2](https://doi.org/10.1175/1520-0493(1993)121<3282:aocowo>2.0.co;2)
- Hauf, T., & Clark, T. L. (1989). Three-dimensional numerical experiments on convectively forced internal gravity waves. *Quarterly Journal of the Royal Meteorological Society*, *115*(486), 309–333. <https://doi.org/10.1002/qj.49711548606>
- Heller, R., Voigt, C., Beaton, S., Dörnbrack, A., Giez, A., Kaufmann, S., et al. (2017). Mountain waves modulate the water vapor distribution in the UTLS. *Atmospheric Chemistry and Physics*, *17*(24), 14853–14869. <https://doi.org/10.5194/acp-17-14853-2017>
- Hersbach, H., Bell, B., Berrisford, P., Biavati, G., Horányi, A., Muñoz Sabater, J., et al. (2018). ERA5 hourly data on pressure levels from 1959 to present [Dataset]. Copernicus Climate Change Service (C3S) Climate Data Store (CDS). <https://doi.org/10.24381/cds.bd0915c6>
- Hersbach, H., Bell, B., Berrisford, P., Hirahara, S., Horányi, A., Muñoz-Sabater, J., et al. (2020). The ERA5 global reanalysis. *Quarterly Journal of the Royal Meteorological Society*, *146*(730), 1999–2049. <https://doi.org/10.1002/qj.3803>
- Hindley, N. P., Smith, N. D., Wright, C. J., Rees, D. A. S., & Mitchell, N. J. (2016). A two-dimensional Stockwell transform for gravity wave analysis of AIRS measurements. *Atmospheric Measurement Techniques*, *9*(6), 2545–2565. <https://doi.org/10.5194/amt-9-2545-2016>
- Jann, A. (2017). Detection of gravity waves in Meteosat imagery by grating cell operators. *European Journal of Remote Sensing*, *50*(1), 509–516. <https://doi.org/10.1080/22797254.2017.1367629>
- Jensen, E. J., Ueyama, R., Pfister, L., Bui, T. V., Alexander, M. J., Podglajen, A., et al. (2016). High-frequency gravity waves and homogeneous ice nucleation in tropical tropopause layer cirrus. *Geophysical Research Letters*, *43*(12), 6629–6635. <https://doi.org/10.1002/2016GL069426>
- Kuettner, J. P., Hildebrand, P. A., & Clark, T. L. (1987). Convection waves: Observations of gravity wave systems over convectively active boundary layers. *Quarterly Journal of the Royal Meteorological Society*, *113*(476), 445–467. <https://doi.org/10.1002/qj.49711347603>
- Lane, T. P., & Clark, T. L. (2002). Gravity waves generated by the dry convective boundary layer: Two-dimensional scale selection and boundary-layer feedback. *Quarterly Journal of the Royal Meteorological Society*, *128*(583), 1543–1570. <https://doi.org/10.1002/qj.200212858308>
- Lane, T. P., Reeder, M. J., & Guest, F. M. (2003). Convectively generated gravity waves observed from radiosonde data taken during MCTEX. *Quarterly Journal of the Royal Meteorological Society*, *129*(590), 1731–1740. <https://doi.org/10.1256/qj.02.196>
- Lane, T. P., Sharman, R. D., Trier, S. B., Fovell, R. G., & Williams, J. K. (2012). Recent advances in the understanding of near-cloud turbulence. *Bulletin of the American Meteorological Society*, *93*(4), 499–515. <https://doi.org/10.1175/BAMS-D-11-00062.1>
- Lyapustin, A., Alexander, M. J., Ott, L., Molod, A., Holben, B., Susskind, J., & Wang, Y. (2014). Observation of mountain lee waves with MODIS NIR column water vapor. *Geophysical Research Letters*, *41*(2), 710–716. <https://doi.org/10.1002/2013GL058770>
- Moustauoui, M., Mahalov, A., Teitelbaum, H., & Grubišić, V. (2010). Nonlinear modulation of O<sub>3</sub> and CO induced by mountain waves in the upper troposphere and lower stratosphere during terrain-induced rotor experiment. *Journal of Geophysical Research*, *115*(D19), D19103. <https://doi.org/10.1029/2009JD013789>
- Nappo, C. J. (2012). The linear theory. In C. J. Nappo (Ed.), *An introduction to atmospheric gravity waves* (Vol. 102, pp. 29–56). Academic Press. <https://doi.org/10.1016/B978-0-12-385223-6.00002-1>
- Podglajen, A., Plougonven, R., Hertzog, A., & Jensen, E. (2018). Impact of gravity waves on the motion and distribution of atmospheric ice particles. *Atmospheric Chemistry and Physics*, *18*(14), 10799–10823. <https://doi.org/10.5194/acp-18-10799-2018>
- Sason, I., & Verdú, S. (2016). *f*-divergence inequalities. *IEEE Transactions on Information Theory*, *62*(11), 5973–6006. <https://doi.org/10.1109/TIT.2016.2603151>
- Schmit, T. J., Griffith, P., Gunshor, M. M., Daniels, J. M., Goodman, S. J., & Lebar, W. J. (2017). A closer look at the ABI on the GOES-R series. *Bulletin of the American Meteorological Society*, *98*(4), 681–698. <https://doi.org/10.1175/BAMS-D-15-00230.1>
- Schmit, T. J., Lindstrom, S. S., Gerth, J. J., Gunshor, M. M., & Gunshor, M. M. (2018). Applications of the 16 spectral bands on the advanced baseline imager (ABI). *Journal of Operational Meteorology*, *6*(4), 33–46. <https://doi.org/10.15191/nwajom.2018.0604>
- Schoeberl, M. R., Jensen, E. J., & Woods, S. (2015). Gravity waves amplify upper tropospheric dehydration by clouds. *Earth and Space Science*, *2*(12), 485–500. <https://doi.org/10.1002/2015EA000127>
- Spichtinger, P., & Krämer, M. (2013). Tropical tropopause ice clouds: A dynamic approach to the mystery of low crystal numbers. *Atmospheric Chemistry and Physics*, *13*(19), 9801–9818. <https://doi.org/10.5194/acp-13-9801-2013>
- Stephan, C. C. (2020). Seasonal modulation of trapped gravity waves and their imprints on trade wind clouds. *Journal of the Atmospheric Sciences*, *77*(9), 2993–3009. <https://doi.org/10.1175/JAS-D-19-0325.1>
- Teixeira, M. A. C. (2014). The physics of orographic gravity wave drag. *Frontiers in Physics*, *2*(43). <https://doi.org/10.3389/fphy.2014.00043>
- Teixeira, M. A. C., & Argain, J. L. (2020). The dependence of mountain wave reflection on the abruptness of atmospheric profile variations. *Quarterly Journal of the Royal Meteorological Society*, *146*(729), 1685–1701. <https://doi.org/10.1002/qj.3760>
- Teixeira, M. A. C., Miranda, P. M. A., Argain, J. L., & Valente, M. A. (2005). Resonant gravity-wave drag enhancement in linear stratified flow over mountains. *Quarterly Journal of the Royal Meteorological Society*, *131*(609), 1795–1814. <https://doi.org/10.1256/qj.04.154>

- Trier, S. B., & Sharman, R. D. (2018). Trapped gravity waves and their association with turbulence in a large thunderstorm anvil during PECAN. *Monthly Weather Review*, *146*(9), 3031–3052. <https://doi.org/10.1175/MWR-D-18-0152.1>
- Uhlenbrock, N. L., Bedka, K. M., Feltz, W. F., & Ackerman, S. A. (2007). Mountain wave signatures in MODIS 6.7- $\mu\text{m}$  imagery and their relation to pilot reports of turbulence. *Weather and Forecasting*, *22*(3), 662–670. <https://doi.org/10.1175/WAF1007.1>
- Wimmers, A., Griffin, S., Gerth, J., Bachmeier, S., & Lindstrom, S. (2018). Observations of gravity waves with high-pass filtering in the new generation of geostationary imagers and their relation to aircraft turbulence. *Weather and Forecasting*, *33*(1), 139–144. <https://doi.org/10.1175/WAF-D-17-0080.1>
- Wright, C. J., Hindley, N. P., Hoffmann, L., Alexander, M. J., & Mitchell, N. J. (2017). Exploring gravity wave characteristics in 3-D using a novel S-transform technique: AIRS/Aqua measurements over the southern Andes and Drake passage. *Atmospheric Chemistry and Physics*, *17*(13), 8553–8575. <https://doi.org/10.5194/acp-17-8553-2017>
- Yao, B., Teng, S., Lai, R., Xu, X., Yin, Y., Shi, C., & Liu, C. (2020). Can atmospheric reanalyses (CRA and ERA5) represent cloud spatiotemporal characteristics? *Atmospheric Research*, *244*, 105091. <https://doi.org/10.1016/j.atmosres.2020.105091>